The HydG Enzyme Generates an $Fe(CO)_2(CN)$ Synthon in Assembly of the FeFe Hydrogenase H-Cluster

Jon M. Kuchenreuther *et al.*

Science **343**, 424 (2014);
DOI: 10.1126/science.1246572

Science (print ISSN 0036-8075; online ISSN 1095-9203) is published weekly, except the last week in December, by the American Association for the Advancement of Science, 1200 New York Avenue NW, Washington, DC 20005.

motion (~1%) of endogenous mRNA (Fig. 1F and fig. S5) than previously reported (22%) (*9*), possibly due to the differences between the endogenous mRNA and the exogenous reporter, or the cell types. Serum-induced localization of β-actin mRNA in fibroblasts appears predominantly mediated by rapid release of stationary mRNA and redistribution into discrete cytoplasmic compartments (fig. S6, movies S2 to S5, and supplementary text), although we cannot rule out short movements driven by nonprocessive motors.

Neuronal RNA transport granules may contain multiple mRNAs (*10*, *11*). To investigate the stoichiometry of β-actin mRNA in hippocampal neurons from MCP×MBS mice, we performed single-molecule FISH (fig. S7). The intensity histograms of diffraction-limited fluorescent spots indicated mRNPs containing multiple copies of β-actin mRNA in the soma and proximal dendrites (fig. S7B), which decreased with distance from the soma (fig. S7D). In live neurons (Fig. 1C and movie S6), ~25% of mRNPs in proximal dendrites contained more than one β-actin mRNA (Fig. 1E). Diffusion of mRNPs in neurons was slower [diffusion coefficient = 3.8 (±0.5) × 10^{-3} $\mu m^2/s$] than in fibroblasts, but ~10% of mRNPs were actively transported anterograde and retrograde (Fig. 1G and fig. S8A) with a mean speed of 1.3 μm/s (fig. S8B). The ratio of anterograde to retrograde transport was 1.1 to 1.5 throughout neuronal development in culture (fig. S8C), which may mediate constitutive delivery into dendrites.

To investigate the activity-dependent dynamics of β-actin mRNA, we imaged live neurons before and after depolarization (60 mM KCl for 3 to 6 min). Pairwise comparisons in the same dendritic regions revealed that there were significant increases in the density of the mRNP particles after KCl depolarization in both cultured neurons (fig. S9) (*8*) and acute brain slices (fig. S10). The diffusion coefficient decreased by a factor of 3 (fig. S9D), and particles with directed motion decreased in both directions (fig. S9E). Therefore, the increase of diffraction-limited spots in the dendrite was not due to transport of mRNA from the soma. We hypothesized that the number of detected spots increased because of the release of mRNAs from mRNP complexes upon stimulation. We quantified the number of β-actin mRNAs contained in each neuronal mRNP by particle intensity. After KCl depolarization, the number of spots containing single β-actin mRNA increased while the number of particles bearing multiple mRNAs decreased (fig. S9B and S10B). We observed merge and split events of particles (Fig. 2, A and B, and movies S7 and S8). Both the split and merge frequencies were reduced after depolarization, but the ratio of split to merge was increased (Fig. 2C). These results suggest that mRNA molecules undergo continuous assembly and disassembly of large mRNP complexes (*12*) but favor the released state upon depolarization, possibly for local translation (*13*, *14*).

We investigated endogenous β-actin gene expression in native tissue by imaging acute brain slices (Fig. 2D). Transcriptional activity was monitored in the hippocampus CA1 region at 20 to 60 μm from the surface before and after KCl depolarization (Fig. 2E). Nascent β-actin mRNA per transcription site increased 10 to 15 min after depolarization (Fig. 2, F and G), likely because of rapid initiation (*15*). Rapid induction of β-actin transcription was observed in various cell lines (*4*, *16*, *17*) but β-actin was not recognized as an immediate early gene in the nervous system, probably because of high basal expression. Increased expression of β-actin may be implicated in transducing synaptic activity into structural plasticity.

The MCP×MBS mouse provides a distinctive tool for monitoring the dynamics of single endogenous mRNA in live mammalian cells and tissues. Our results with the β-actin gene suggest that the technique could be generally applicable to other genes to investigate the effect of the tissue microenvironment on single-cell gene expression.

References and Notes

1. S. Tyagi, *Nat. Methods* **6**, 331–338 (2009).
2. E. Bertrand *et al.*, *Mol. Cell* **2**, 437–445 (1998).
3. C. Lois, E. J. Hong, S. Pease, E. J. Brown, D. Baltimore, *Science* **295**, 868–872 (2002).
4. T. Lionnet *et al.*, *Nat. Methods* **8**, 165–170 (2011).
5. T. M. Bunnell, B. J. Burbach, Y. Shimizu, J. M. Ervasti, *Mol. Biol. Cell* **22**, 4047–4058 (2011).
6. J. B. Lawrence, R. H. Singer, *Cell* **45**, 407–415 (1986).
7. G. J. Bassell *et al.*, *J. Neurosci.* **18**, 251–265 (1998).
8. D. M. Tiruchinapalli *et al.*, *J. Neurosci.* **23**, 3251–3261 (2003).
9. D. Fusco *et al.*, *Curr. Biol.* **13**, 161–167 (2003).
10. K. Ainger *et al.*, *J. Cell Biol.* **123**, 431–441 (1993).
11. R. B. Knowles *et al.*, *J. Neurosci.* **16**, 7812–7820 (1996).
12. C. P. Brangwynne *et al.*, *Science* **324**, 1729–1732 (2009).
13. A. M. Krichevsky, K. S. Kosik, *Neuron* **32**, 683–696 (2001).
14. A. R. Buxbaum, B. Wu, R. H. Singer, *Science* **343**, 419–422 (2014).
15. D. R. Larson, D. Zenklusen, B. Wu, J. A. Chao, R. H. Singer, *Science* **332**, 475–478 (2011).
16. A. M. Femino, F. S. Fay, K. Fogarty, R. H. Singer, *Science* **280**, 585–590 (1998).
17. M. E. Greenberg, E. B. Ziff, L. A. Greene, *Science* **234**, 80–83 (1986).

Acknowledgments: Supported by NIH grants EB13571 and NS083085-19 (formerly GM84364) (R.H.S.) and National Research Service Award F32-GM87122 and the Integrated Imaging Program (H.Y.P.).

Supplementary Materials

www.sciencemag.org/content/343/6169/422/suppl/DC1
Materials and Methods
Supplementary Text
Figs. S1 to S10
Movies S1 to S8
References (*18*–*36*)

16 April 2013; accepted 15 October 2013
10.1126/science.1239200

The HydG Enzyme Generates an $Fe(CO)_2(CN)$ Synthon in Assembly of the FeFe Hydrogenase H-Cluster

Jon M. Kuchenreuther,[1]* William K. Myers,[1]* Daniel L. M. Suess,[1] Troy A. Stich,[1] Vladimir Pelmenschikov,[2] Stacey A. Shiigi,[3] Stephen P. Cramer,[1,4] James R. Swartz,[3,5] R. David Britt,[1]† Simon J. George[1]†

Three iron-sulfur proteins—HydE, HydF, and HydG—play a key role in the synthesis of the $[2Fe]_H$ component of the catalytic H-cluster of FeFe hydrogenase. The radical *S*-adenosyl-L-methionine enzyme HydG lyses free tyrosine to produce *p*-cresol and the CO and CN^- ligands of the $[2Fe]_H$ cluster. Here, we applied stopped-flow Fourier transform infrared and electron-nuclear double resonance spectroscopies to probe the formation of HydG-bound Fe-containing species bearing CO and CN^- ligands with spectroscopic signatures that evolve on the 1- to 1000-second time scale. Through study of the ^{13}C, ^{15}N, and ^{57}Fe isotopologs of these intermediates and products, we identify the final HydG-bound species as an organometallic $Fe(CO)_2(CN)$ synthon that is ultimately transferred to apohydrogenase to form the $[2Fe]_H$ component of the H-cluster.

FeFe hydrogenase enzymes rapidly evolve H_2 at a 6-Fe catalytic site termed the H-cluster (Fig. 1A) (*1*–*3*), which comprises a traditional 4Fe-4S subcluster ($[4Fe\text{-}4S]_H$), produced by canonical Fe-S cluster biosynthesis proteins, that is linked via a cysteine bridge to a dinuclear Fe subcluster ($[2Fe]_H$) that contains unusual ligands. Specifically, the $[2Fe]_H$ subcluster possesses two terminal CN^- ligands, two terminal CO ligands, and azadithiolate and CO bridges, all of which are thought to be synthesized and installed by a set of Fe-S proteins denoted HydE, HydF, and HydG. In one recent model for the $[2Fe]_H$ subcluster bioassembly pathway (*4*, *5*), the two radical *S*-adenosyl-L-methionine (SAM) enzymes of the set, HydE and HydG, generate the dithiolate moiety and free CO and CN^-, respectively, and these ligands are then transferred to a dinuclear Fe precursor bound to HydF,

[1]Department of Chemistry, University of California, Davis, Davis, CA 95616, USA. [2]Institut für Chemie, Technische Universität Berlin, Berlin 10623, Germany. [3]Department of Bioengineering, Stanford University, Stanford, CA 94305, USA. [4]Physical Biosciences Division, Lawrence Berkeley National Laboratory, Berkeley, CA 94720, USA. [5]Department of Chemical Engineering, Stanford University, Stanford, CA 94305, USA.

*These authors contributed equally to this work.
†Corresponding author. E-mail: rdbritt@ucdavis.edu (R.D.B.); sjgeorge@ucdavis.edu (S.J.G.)

which acts as a scaffold protein for assembling the final $[2Fe]_H$ subunit. Individually expressed HydE, HydF, and HydG can be combined for successful in vitro synthesis of the $[2Fe]_H$ component of the H-cluster and concurrent activation of FeFe hydrogenase apoprotein (*6*, *7*). Alternatively, an abiotically synthesized dinuclear Fe subcluster, constructed with an azadithiolate bridge as well as one CN^- and two CO ligands per Fe,

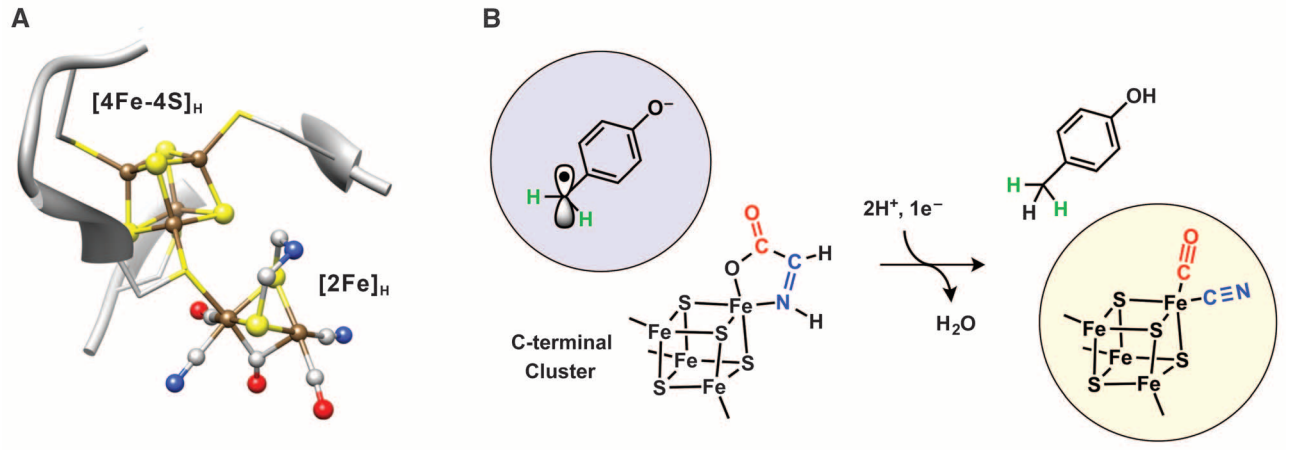

Fig. 1. Ligand synthesis by HydG. (**A**) The catalytic H-cluster of FeFe hydrogenases. Ball-and-stick representation (from Protein Data Bank entry 3C8Y) was generated by using University of California San Francisco Chimera: Fe (brown), S (yellow), C (gray), O (red), and N (blue). H was not shown for simplicity. (**B**) Proposed HydG-catalyzed conversion of 4Fe-4S–bound DHG to an Fe(CO)(CN) species concomitant with conversion of 4OB• to *p*-cresol (*17*).

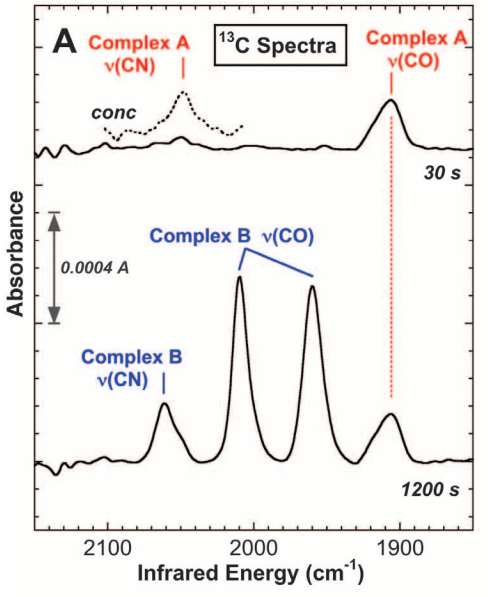

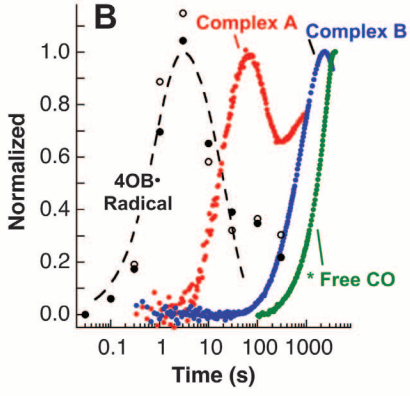

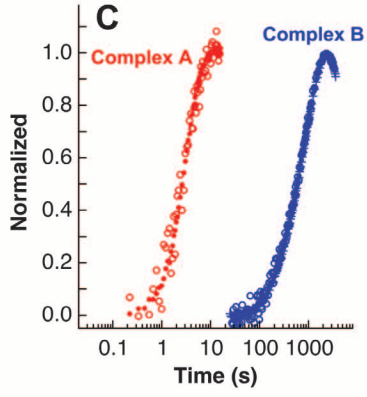

D	Mode	^{12}C (cm^{-1})	^{13}C (cm^{-1})
Complex A	ν(CO)	1949	1906
	ν(CN)	2093	2048
Complex B	ν(CO)	2005	1960
	ν(CO)	2057	2010
	ν(CN)	2106	2062

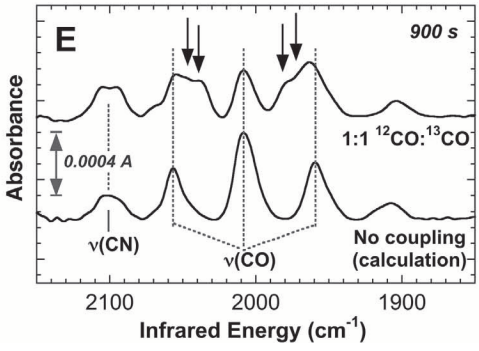

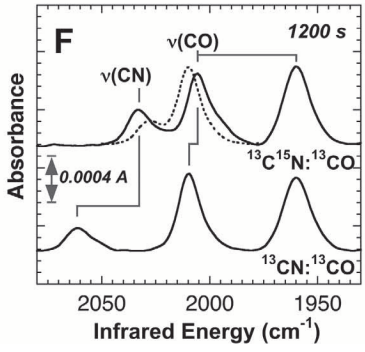

Fig. 2. FTIR spectra. Reactions used 100 μM $HydG^{WT}$ and $(^{13}C)_9$-Tyr, producing ^{13}CO and ^{13}CN ligands, unless indicated otherwise. (**A**) SF-FTIR spectra measured at 30 and 1200 s (solid lines) and at 10 s using 800 μM $HydG^{WT}$ (dotted line, plotted at half intensity). (**B**) Time dependence of formation and decay of the following species: 4OB• determined by EPR spectroscopy, two experimental runs (•, ○) and corresponding kinetic fit (dashed line) (*17*); FTIR data (no kinetic fit) of complex A (red) and complex B (blue) determined by the peak heights of their respective ν(CO) modes [see (A)]; and free CO trapped by myoglobin (green) (fig. S3). Each data set is scaled to unity at its maximum value. (**C**) Comparison of the time dependence of the peak heights of all ν(CO) and ν(CN) bands for complex A and complex B. Complex A red symbols are as follows: ○, ν(^{13}CN); •, ν(^{13}CO). Complex B blue symbols are as follows: ○, ν(^{13}CN); •, ν(^{13}CO) 2010 cm^{-1}; +, ν(^{13}CO) 1960 cm^{-1}. The data for complex A were taken from measurements by using 800 μM $HydG^{WT}$ in order to enhance the signal:noise ratio of the ν(CN) mode. (**D**) Table of frequencies for observed IR bands of complexes A and B prepared by using Tyr (middle column) or $(^{13}C)_9$-Tyr (right-most column). (**E**) SF-FTIR spectrum of complex B measured at 900 s and prepared by using a 1:1 mixture of Tyr and ^{13}COO-Tyr (top). Average of the ^{12}CO and ^{13}CO product B spectra (bottom). The arrows indicate new bands not present in either the ^{12}CO or ^{13}CO spectra of complex B. (**F**) SF-FTIR spectra of complex B measured at 1200 s and prepared by using $(^{13}C)_9{}^{15}N$-Tyr (top) and $(^{13}C)_9$Tyr (bottom). Expected CN and CO bands for $^{13}C^{15}N$-containing complex B in the absence of ν(CN)/ν(CO) vibrational mixing (dotted line). Predicted band shifts computed simply by the change in the reduced mass.

can also be used to activate FeFe hydrogenase (*8*, *9*).

The HydG radical SAM enzyme was previously reported to use free L-tyrosine (Tyr) as its substrate to generate *p*-cresol and free CO and CN^- as its products (*6*, *10*–*12*). Although HydG has yet to be crystallographically characterized, sequence analysis and results from spectroscopic studies indicate that it has two 4Fe-4S clusters, each with distinct functions (*13*, *14*). The SAM-binding 4Fe-4S cluster, located near the N terminus, reductively cleaves SAM, producing methionine plus a strongly oxidizing 5′-deoxyadenosyl radical (5′-dA$^\bullet$) (*15*, *16*). The second Fe-S cluster, located near the C terminus, was implicated as the site of Tyr binding in our recent investigation of the HydG reaction mechanism using electron paramagnetic resonance (EPR) spectroscopy (*17*). Also on the basis of EPR spectroscopic results, we proposed that the initial 5′-dA$^\bullet$ generates a neutral tyrosine radical bound to this C-terminal 4Fe-4S cluster, which then undergoes heterolytic cleavage at the C_α-C_β bond, forming a 4-oxidobenzyl radical (4OB$^\bullet$) and cluster-bound dehydroglycine (DHG) (Fig. 1B) (*17*). Electron and proton transfer to 4OB$^\bullet$ then yields the *p*-cresol product concomitant with the scission of DHG to form Fe-bound CO and CN^- and water (Fig. 1B). In this report, we explored the subsequent time course of the HydG reaction by using stopped-flow Fourier transform infrared (SF-FTIR) and electron-nuclear double resonance (ENDOR) spectroscopies to follow the synthesis of $Fe(CO)_x(CN)_y$ species and track them to the completion of the H-cluster bioassembly pathway.

SF-FTIR is a useful time-resolved method for studying the HydG reaction mechanism because CO and CN^- ligands give rise to strong infrared absorption bands with energies and intensities sensitive to the coordination and electronic environment of the bound Fe center. Figure 2 summarizes SF-FTIR data after the reaction of wild-type *Shewanella oneidensis* HydG ($HydG^{WT}$) with excess substrates SAM and ^{13}C-labeled Tyr [$(^{13}C)_9$-Tyr] in the presence of the reductant sodium dithionite (DTH). Observed bands are assigned to stretch vibrations of CO and CN ligands on the basis of their energy shifts upon ^{12}C:^{13}C and ^{14}N:^{15}N site-specific isotope substitution (fig. S2), which was achieved through use of the appropriate Tyr isotopologs (*6*). The time evolution of the resultant spectra (Fig. 2, A to C) reveals a stepwise conversion of a discrete intermediate, which we term complex A, to a distinct new species, complex B. Complex A is characterized by two bands at 1906 cm^{-1} and 2048 cm^{-1} [1949 cm^{-1} and 2093 cm^{-1} with ^{12}C-Tyr (Fig. 2D)], which we assign to stretching modes arising from terminal Fe-^{13}CO and Fe-^{13}CN moieties, respectively. The kinetic profile (Fig. 2B) shows that complex A accumulates on the same time scale as the decay of the previously observed 4OB$^\bullet$ (*17*). Hence, the FTIR spectrum and formation kinetics of complex A are consistent with the mechanistic model in Fig. 1B, with the first turnover of HydG, SAM, and Tyr forming bound CO and CN^-, presumably on the unique Fe site of the C-terminal 4Fe-4S cluster. Complex A does not form in the relatively conservative Cys^{394}→Ser^{394} (C394S), C397S HydG double mutant ($HydG^{SxxS}$), which lacks the C-terminal cluster (figs. S3 and S4).

Complex A reaches a maximum concentration and starts to decay after about 30 s, concomitant with the appearance and growth of complex B. The three bands associated with complex B have identical kinetics and may be assigned to terminally bound ligands: two high-energy, predominately ν(^{13}CO) modes at 1960 cm^{-1} and 2010 cm^{-1} and a ν(^{13}CN) mode at 2062 cm^{-1}. We assign the 2010 cm^{-1} band to a predominantly ν(^{13}CO) mode rather than a ν(^{13}CN) mode because its energy shifts upon ^{13}C isotopic substitution at the carboxyl position in Tyr [the moiety that gives rise to the CO but not the CN ligands in the mature H cluster (fig. S2)] (*6*). An additional band at 1906 cm^{-1} and shoulder at 2048 cm^{-1} likely arise from residual complex A.

A reasonable structure for complex B is a cuboidal $Fe(CO)_2(CN)$-[3Fe-4S] species in which the unique Fe site is coordinated by the three Tyr-derived diatomic ligands. For CO and CN^- ligands that are bound to a single Fe center, the ν(CO) and ν(CN) vibrational modes are expected to be strongly coupled. To test for vibrational mixing between the two observed ν(CO) frequencies, we generated a 1:2:1 mixture of $^{12}CO^{12}CO$-, $^{12}CO^{13}CO$-, and $^{13}CO^{13}CO$-labeled complex B from a 1:1 mixture of natural abundance Tyr and ^{13}COO-Tyr. If the two ν(CO) modes in complex B were not coupled, then the expected resulting spectrum would be a simple 1:1 superposition of the $^{12}CO^{12}CO$ and $^{13}CO^{13}CO$ spectra (Fig. 2E, lower trace). Instead, the observed spectrum displayed additional, overlapping bands (Fig. 2E, upper trace) that can be ascribed to the two $^{12}CO^{13}CO$-labeled isotopomers with apparent CO-stretching frequencies shifted relative to their

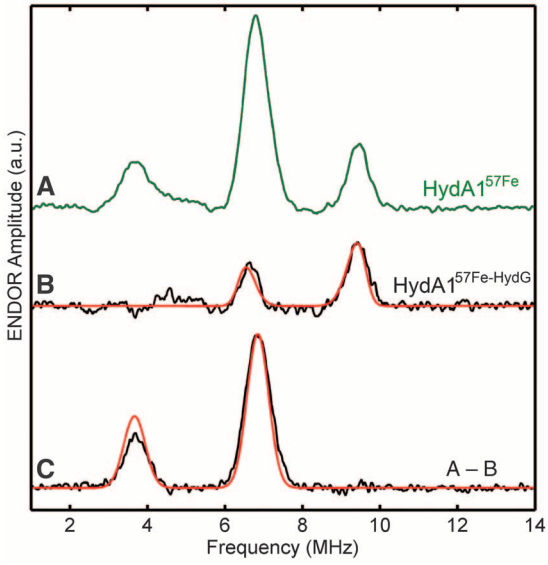

Fig. 3. *Q*-band (34.00 GHz, 1.155 T) Davies ENDOR spectra of FeFe hydrogenase HydA1 enriched with ^{57}Fe. (**A**) $HydA1^{57Fe}$; (**B**) $HydA1^{57Fe–HydG}$ [black, experiment; red, simulation with $A(^{57}Fe)$ = 16.0 MHz]; (**C**) (A) − (B) difference spectrum [black, experiment; red, simulation with $A(^{57}Fe)$ = 10.55 MHz]. ENDOR simulations used line widths of 0.4 and 0.65 MHz for $[2Fe]_H$ and $[4Fe\text{-}4S]_H$ components, respectively, with other values taken directly from experiment parameters and CW EPR simulations. The ENDOR spectrum of natural abundance Fe HydA1 in the H_{ox} state was subtracted from both spectra (A) and (B). a.u., arbitrary units.

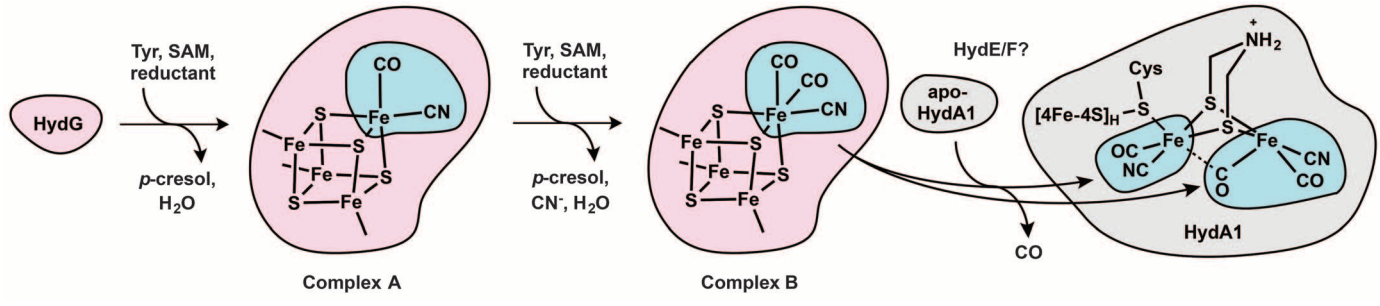

Fig. 4. Schematic for the bioassembly of the FeFe hydrogenase H-cluster via a HydG-synthesized $Fe(CO)_2(CN)$ synthon. Pink indicates HydG; cyan, the unique Fe site of HydG that is installed into apo HydA1; gray, HydA1.

isotopically pure counterparts because of vibrational mixing of the two fundamental ν(CO) modes (fig. S6). Similarly, a comparison of spectra generated by using $(^{13}C)_9$-Tyr and $(^{13}C)_9{}^{15}N$-Tyr (Fig. 2F) shows that ^{15}N substitution produces both a smaller than expected energy shift in the ν(CN) mode as well as an energy shift in the higher energy ν(CO) mode, indicating that these modes are also vibrationally mixed. Taken together, these coupling data suggest that all three ligands (two CO and one CN^-) in complex B are bound to a single Fe-center.

The relatively high energies of the ν(CO) modes of complex B suggest that it may be appropriately modeled as a cationic, low-spin $[Fe(II)(CO)_2(CN)]^+$ complex based on comparisons with related neutral, low-spin $Fe(II)(CO)_2(CN)$ complexes (*18*, *19*). The density functional theory (DFT)–calculated ν(CO) and ν(CN) frequencies and intensities of $[fac\text{-}(H_2S)_3Fe(II)(CO)_2(CN)]^+$, a simple model for $\{Fe(II)(CO)_2(CN)\text{-}[3Fe\text{-}4S]\}^+$, show reasonable agreement with the observed spectrum of complex B (fig. S5 and table S2). Alternative structures in which the CO and CN^- ligands are not cofacial or in which the sulfur donors are replaced with oxygen donors were not found to give rise to the expected intensity patterns. In addition, the coupling pattern in the $^{12}CO^{13}CO$ isotope mixture (Fig. 2E, top) was only reproduced computationally when the two CO ligands have different inherent ν(CO) energies, which could be explained by the electronic asymmetry of the coordinating $[3Fe\text{-}4S]^0$ subcluster (*20*) or by asymmetry in CO H-bonding interactions.

The kinetics in Fig. 2B suggest sequential conversion of complex A to complex B, which we associate with another turnover of HydG acting on a second substrate Tyr to form an additional CO to coordinate the unique Fe center of the C-terminal cluster (*21*). Unlike the first turnover (*17*), we have no experimental information at this time about how Tyr binds and what intermediates may be involved in this second reaction, although we note that our model for complex A is coordinatively unsaturated and could bind Tyr or a Tyr-derived fragment during the second turnover. Only at much longer times was free CO detected in solution through its binding to exogenous myoglobin (see green trace in Fig. 2B and fig. S3), which rules out the binding of externally derived CO as part of the mechanism. The release of free CO is correlated with the rise of complex A (Fig. 2B) at a late time (>300 s), suggesting that complex B may degrade to complex A by loss of CO when other H-cluster maturation components are not available to facilitate its incorporation into the proper downstream assembly products (vide infra). Reports of no lag phase in free CO production (*12*) may arise from alternative chemistry resulting from differences in experimental protocols.

To determine the fate of the Fe-containing complex B, we measured the continuous-wave (CW) EPR and pulse ENDOR spectra of HydA1 hydrogenase from *Chlamydomonas reinhardtii* that had been either uniformly or selectively labeled with ^{57}Fe (nuclear spin, $I = 1/2$). Uniformly ^{57}Fe-labeled HydA1 ($HydA1^{57Fe}$) was generated by introducing ^{57}Fe into the growth media for HydA1. The *Q*-band Davies pulse ENDOR (*22*) spectrum of the purified $HydA1^{57Fe}$ poised in the H_{ox} state is shown in Fig. 3A. This spectrum was obtained at the highest electron *g* value, $g_1 = 2.10$, where there is no overlap with the EPR signal from the CO-inhibited H_{ox}-CO form (fig. S7), and it shows several peaks in the 3- to 10-MHz range.

In order to determine whether Fe from the HydG cluster is transferred to the HydA1 hydrogenase, we evaluated a sample of HydA1 (that we term $HydA1^{57Fe\text{–}HydG}$) in which the $[2Fe]_H$ subcluster was assembled in vitro (*6*, *7*) by using HydE and HydF expressed in natural abundance media and HydG expressed in ^{57}Fe-enriched media (fig. S1). The corresponding ENDOR spectrum (Fig. 3B) was well simulated by a single doublet, with frequencies $\nu_\pm = A(^{57}Fe)/2 \pm \nu_I$, where $A(^{57}Fe) = 16.0$ MHz is the effective hyperfine tensor component at this $g_1 = 2.10$ value and ν_I is the ^{57}Fe nuclear Zeeman frequency at this magnetic field. We assigned this doublet to the $[2Fe]_H$ subcluster, because the $[4Fe\text{-}4S]_H$ subcluster is not labeled with ^{57}Fe for this sample. Subtraction of the ^{57}Fe ENDOR spectrum of the $[2Fe]_H$ subcluster–labeled sample from that of the $HydA1^{57Fe}$ sample isolated the ^{57}Fe ENDOR signal that arose from the $[4Fe\text{-}4S]_H$ cluster (Fig. 3C). This difference spectrum was well simulated as an ENDOR doublet with $A(^{57}Fe) = 10.55$ MHz. Both $A(^{57}Fe)$ values for HydA1 are consistent with previous ENDOR and Mössbauer spectroscopic studies of the H_{ox} state of *Desulfovibrio vulgaris* and *Clostridium pasteurianum* hydrogenases (≈16 to 18 MHz for the $[2Fe]_H$ subcluster and ≈8 to 10 MHz for the $[4Fe\text{-}4S]_H$ cluster) (*23*–*26*), although they differ somewhat from those derived from ENDOR data for the *Desulfovibrio desulfuricans* hydrogenase (12.4 and 11.1 MHz, respectively) (*27*). Comparing the magnitudes of the two $A(^{57}Fe)$ values determined above confirms that the greatest spin density of the H-cluster in the H_{ox} state lies on the $[2Fe]_H$ subcluster. More importantly, these ENDOR data show that Fe in the $[2Fe]_H$ subcluster of the mature H-cluster originates from the HydG radical SAM maturase.

The SF-FTIR and ^{57}Fe ENDOR spectroscopic results presented in this report provide further insight into the assembly of the $[2Fe]_H$ subcluster of FeFe hydrogenase, illustrated in Fig. 4. Prior work demonstrated that the CO and CN^- ligands of the $[2Fe]_H$ subcluster are generated from Tyr via HydG. Results from SF-FTIR spectroscopic studies provide evidence for the formation of two distinct Fe-bound CO- and CN-containing species, complexes A and B, during the HydG reaction. Analysis of the vibrational mode coupling, buttressed by DFT studies on model complexes, lead us to postulate that complex B is a 3Fe-4S–bound $Fe(CO)_2(CN)$ species. The ^{57}Fe-labeling experiments prove that Fe in the $[2Fe]_H$ subcluster is provided by HydG. It is therefore straightforward to envisage a mechanism wherein two complex B units assemble together with a dithiolate bridge to form the $[2Fe]_H$ subcluster. Our proposal for the structure of this deliverable species is consistent with all of the available data and points to the biologically relevant product of the HydG reaction as being an organometallic $Fe(CO)_2(CN)$ synthon.

References and Notes

1. P. M. Vignais, B. Billoud, *Chem. Rev.* **107**, 4206–4272 (2007).
2. K. A. Vincent, A. Parkin, F. A. Armstrong, *Chem. Rev.* **107**, 4366–4413 (2007).
3. M. W. W. Adams, E. I. Stiefel, *Curr. Opin. Chem. Biol.* **4**, 214–220 (2000).
4. E. M. Shepard *et al.*, *Proc. Natl. Acad. Sci. U.S.A.* **107**, 10448–10453 (2010).
5. D. W. Mulder *et al.*, *Structure* **19**, 1038–1052 (2011).
6. J. M. Kuchenreuther, S. J. George, C. S. Grady-Smith, S. P. Cramer, J. R. Swartz, *PLOS ONE* **6**, e20346 (2011).
7. J. M. Kuchenreuther, R. D. Britt, J. R. Swartz, *PLOS ONE* **7**, e45850 (2012).
8. G. Berggren *et al.*, *Nature* **499**, 66–69 (2013).
9. J. Esselborn *et al.*, *Nat. Chem. Biol.* **9**, 607–609 (2013).
10. E. Pilet *et al.*, *FEBS Lett.* **583**, 506–511 (2009).
11. R. C. Driesener *et al.*, *Angew. Chem. Int. Ed.* **49**, 1687–1690 (2010).
12. E. M. Shepard *et al.*, *J. Am. Chem. Soc.* **132**, 9247–9249 (2010).
13. J. K. Rubach, X. Brazzolotto, J. Gaillard, M. Fontecave, *FEBS Lett.* **579**, 5055–5060 (2005).
14. C. Tron *et al.*, *Eur. J. Inorg. Chem.* **2011**, 1121–1127 (2011).
15. P. A. Frey, A. D. Hegeman, F. J. Ruzicka, *Crit. Rev. Biochem. Mol. Biol.* **43**, 63–88 (2008).
16. J. L. Vey, C. L. Drennan, *Chem. Rev.* **111**, 2487–2506 (2011).
17. J. M. Kuchenreuther *et al.*, *Science* **342**, 472–475 (2013).
18. T. S. Piper, F. A. Cotton, G. Wilkinson, *J. Inorg. Nucl. Chem.* **1**, 165–174 (1955).
19. D. J. Darensbourg, *Inorg. Chem.* **11**, 1606–1609 (1972).
20. J. A. Weigel, R. H. Holm, K. K. Surerus, E. Munck, *J. Am. Chem. Soc.* **111**, 9246–9247 (1989).
21. This process would also entail formal loss of CN^-. Although the SF-FTIR data for complex B cannot rigorously exclude coordination by two CN^- groups, we consider this to be unlikely because only one ν(CN) mode is observed and only one CN^- per Fe is present in both the assembled $[2Fe]_H$ subcluster and the synthetic dinuclear Fe compound that can activate the FeFe hydrogenase (*8*, *9*).
22. E. R. Davies, *Phys. Lett. A* **47**, 1–2 (1974).
23. J. Telser, M. J. Benecky, M. W. W. Adams, L. E. Mortenson, B. M. Hoffman, *J. Biol. Chem.* **261**, 13536–13541 (1986).
24. J. Telser, M. J. Benecky, M. W. W. Adams, L. E. Mortenson, B. M. Hoffman, *J. Biol. Chem.* **262**, 6589–6594 (1987).
25. C. V. Popescu, E. Munck, *J. Am. Chem. Soc.* **121**, 7877–7884 (1999).
26. A. S. Pereira, P. Tavares, I. Moura, J. J. G. Moura, B. H. Huynh, *J. Am. Chem. Soc.* **123**, 2771–2782 (2001).
27. A. Silakov, E. J. Reijerse, S. P. J. Albracht, E. C. Hatchikian, W. Lubitz, *J. Am. Chem. Soc.* **129**, 11447–11458 (2007).

Acknowledgments: This work was funded by the NIH (R.D.B., no GM072623; S.P.C., no. GM65440) and by the Division of Material Sciences and Engineering (J.R.S., award no. DE-FG02-09ER46632) of the Office of Basic Energy Sciences of the U.S. Department of Energy (DOE), by the Office of Biological and Environmental Research of the DOE (S.P.C.), and the UniCat Cluster of Excellence of the German Research Council (V.P.).

Supplementary Materials

www.sciencemag.org/content/343/6169/424/suppl/DC1
Materials and Methods
Figs. S1 to S10
Tables S1 and S2
References (*28*–*43*)

30 September 2013; accepted 9 December 2013
10.1126/science.1246572